POLITECNICO DI TORINO
Repository ISTITUZIONALE

Injectionless Sensorless Control of Synchronous Reluctance Machine for Zero to Low Speeds Region

Original
Injectionless Sensorless Control of Synchronous Reluctance Machine for Zero to Low Speeds Region / Varatharajan, A., Pescetto, P., Pellegrino, G.. - (2018). (International Symposium on Sensorless Control for Electrical Drives (SLED) Helsinki, Finland September 13-14) [10.1109/SLED.2018.8486061].

Availability:
This version is available at: 11583/2712434 since: 2020-01-30T14:58:00Z

Publisher:
IEEE

Published
DOI:10.1109/SLED.2018.8486061

Terms of use:

This article is made available under terms and conditions as specified in the corresponding bibliographic description in the repository

Publisher copyright
IEEE postprint/Author's Accepted Manuscript

©2018 IEEE. Personal use of this material is permitted. Permission from IEEE must be obtained for all other uses, in any current or future media, including reprinting/republishing this material for advertising or promotional purposes, creating new collecting works, for resale or lists, or reuse of any copyrighted component of this work in other works.

(Article begins on next page)

19 November 2026

Injectionless Sensorless Control of Synchronous Reluctance Machine for Zero to Low Speeds Region

Anantaram Varatharajan
Department of Energy
Politecnico di Torino
Torino, Italy
anantaram.varatharajan@polito.it

Paolo Pescetto
Department of Energy
Politecnico di Torino
Torino, Italy
paolo.pescetto@polito.it

Gianmario Pellegrino
Department of Energy
Politecnico di Torino
Torino, Italy
gianmario.pellegrino@polito.it

***Abstract*—An alternative to the high frequency injection approach for sensorless control at zero and low speed region is proposed for synchronous reluctance machines (SyR) using finite-control-set model predictive control (FCS-MPC). The saliency based position estimate aims to exploit the switching current ripple which is pronounced owing to the nature of MPC especially around zero and low speed region due to the minimal back-emf. A demerit of the high frequency injection techniques is the bandwidth hindrance of position observer by the demodulating low pass filter (LPF). In the proposed method, no such filters are required and consequently, high bandwidth is achieved. Guidelines for the calibration of observers are addressed. In addition, the effects of cross-saturation on position estimation is inherently considered. The experimental validation on a 1 kW SyR shows stable operation under torque and speed transients, and proves the feasibility of the proposed technique.**

***Index Terms*—Sensorless control, synchronous reluctance machines, model predictive control**

I. Introduction

The proliferation of SyR in the recent years is attributed to its properties such as low cost, ruggedness and high efficiency. Moreover, SyR have optimized flux barriers to achieve low torque ripple which makes it strongly competitive against induction machines. In addition, the saliency can be exploited for sensorless applications.

The literature presents several well-established techniques for position estimation based on back-emf which are robust at medium and high speeds but have questionable reliance at low speeds and all of them fail at standstill. Numerous studies have been directed at high frequency injection in the form of rotating or pulsating signals in various reference frames for low speeds position estimation [1] [2]. Besides the acoustic noise, the high frequency injection constrains the voltage bandwidth affecting the dynamic performance. Moreover, the addition of LPF in the demodulation stage hinders the bandwidth of position observer. [3] provides a comprehensive review of literature on sensorless control techniques.

To refrain from LPF, several current derivative based position estimation techniques have been studied: [4] proposes a modified PWM pattern for INFORM method with over sampling while [5] involves periodic test voltage space vector injection. To this end, very high frequency square-wave voltage injection has been investigated: [6] uses a rotating injection at one third the sampling frequency while [7] injects pulsating voltage in d axis at half the sampling frequency; however, their feasibility is limited to low inductance machines in the order of few mH as the amplitude of injected voltage is a limiting factor. Conversely, finite control set predictive control assists current derivatives/ripples based approach as the full dc-link voltage appears across the motor terminals in a control period due to absence of modulators. [8] uses model predictive current control where the error signal is calculated from the back-emf component and hence is inadequate for low speeds operation. Predictive torque control is used in [9] where the position error signal is computed in stationary reference frame, which increases complexity, and employs additional angle compensation curve to compensate for cross-saturation effects. The position error is observed to be quite large in the bounds of $\pm 20^\circ$. This paper has similar philosophy but differs in that the estimation is performed in dq coordinates, which simplifies the expressions, and the cross-saturation effect is inherently taken into account. Position estimation in stationary reference frame with MPC for IPMSM is proposed in [10] which overlooks the impact of saturation and cross-saturation properties and is computationally elaborate. An optimization solver is used in [11] for MPC based position estimation which has a demerit of high steady-state error $> 10^\circ$ at load resulting from saturation effects that are not considered. The results obtained do not justify the computational effort.

This paper proposes a FCS-MPC based sensorless control where the position error is evaluated in dq reference frame

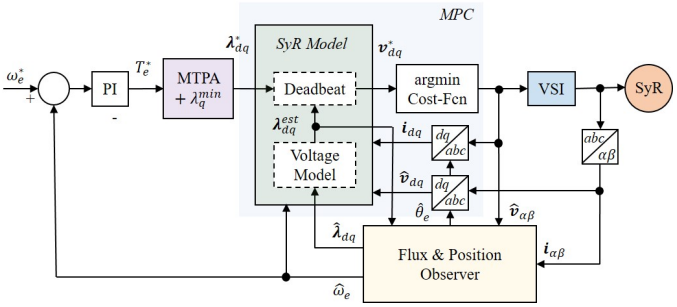


Fig. 1. Block diagram of control system

from the discrepancy in the flux estimation between voltage and current models. Owing to the amalgamation of position observer with the hybrid flux observer (HFO), a simplified expression is obtained that is intuitive and computationally inexpensive. In addition, the technique has been developed to extend the applicability to not merely low but also moderately high inductance machines. The benefits of the high bandwidth of position observer are highlighted and guidelines for tuning the regulators are elucidated, making it compatible with plug & play and self-commissioning systems. The following chapter talks about the machine model, notations and the predictive control scheme. Chapter 3 introduces the sensorless control, working principle and calibration of tracking loop. Chapter 4 contains the experimental validation followed by concluding comments.

II. Finite Control Set - Model Predictive Control

The motor model and the predictive control system is briefly discussed to introduce the notations. Real space vectors will be used in stationary $(\alpha\beta)$ and rotor (dq) reference frame; for example, the stator current is $\boldsymbol{i}_{dq} = [i_d, i_q]^T$ where i_d and i_q are the components of the vector in dq reference frame. The orthogonal rotational matrix is $\mathbf{J} = \left[\begin{smallmatrix} 0 & -1 \\ 1 & 0 \end{smallmatrix}\right]$. An overview of the control system is illustrated in the block diagram, Fig. 1.

A. Mathematical model of SyR

The stator voltage of a synchronous reluctance machine is

$$\boldsymbol{v}_{dq} = R_s \boldsymbol{i}_{dq} + \frac{d\boldsymbol{\lambda}_{dq}}{dt} + \omega_e \mathbf{J}\, \boldsymbol{\lambda}_{dq} \tag{1}$$

where R_s is the stator resistance, $\boldsymbol{\lambda}_{dq}$ is the stator flux linkages and $\omega_e = d\theta_e/dt$ is the electrical angular velocity. The incremental inductance matrix $\mathbf{L}^{inc}$ is defined as

$$d\boldsymbol{\lambda}_{dq} = \boldsymbol{L}^{inc}\, d\boldsymbol{i}_{dq} \qquad \boldsymbol{L}^{inc} = \begin{bmatrix} l_d & l_{dq} \\ l_{dq} & l_q \end{bmatrix} \tag{2}$$

where l_d, l_q represents the incremental inductance along d and q axis respectively while l_{dq} is the cross-saturation component. The electromagnetic torque is

$$T_e = \frac{3p}{2}(\boldsymbol{\lambda}_{dq} \times \boldsymbol{i}_{dq}) \tag{3}$$

where p is the number of pole pairs.

B. Model predictive control scheme

The superscript $\hat{}$ represents estimated quantities. The stator flux linkage $\hat{\boldsymbol{\lambda}}_{dq}(k)$ is obtained from the HFO. It relies on flux linkage maps $\boldsymbol{f}_{dq}(\boldsymbol{i}_{dq})$ based current model (CM) at low speeds and transitions into the voltage model (VM) at high speeds, crossing over at the frequency g rad/s (4).

$$\hat{\boldsymbol{\lambda}}_{\alpha\beta} = \frac{s}{s+g}\frac{\boldsymbol{v}_{\alpha\beta} - R_s \boldsymbol{i}_{\alpha\beta}}{s} + \frac{g}{s+g}\, \mathrm{e}^{-j\theta} \boldsymbol{f}_{dq}(\boldsymbol{i}_{dq})\,((k)) \tag{4}$$

where s is the Laplace variable. The cross-over frequency is set to $g = 2\pi \cdot 10$ rad/s. The experimentally identified flux linkage maps of the SyR motor under test is shown in Fig. 2.

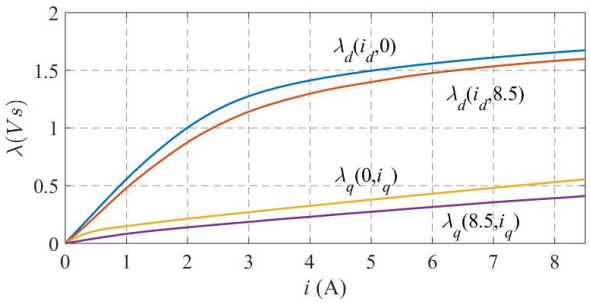


Fig. 2. Flux linkage of 2.2 kW SyR motor under test

The key equations pertaining to a deadbeat type FCS-MPC in dq synchronous rotor reference frame are discussed in (5)-(8). To account for the digital delay, the state variables λ_d, λ_q are estimated for the next sampling instant, $k+1^{th}$, according to (5).

$$\boldsymbol{\lambda}_{dq}^{est}(k+1) = \hat{\boldsymbol{\lambda}}_{dq}(k) + T_s[\hat{\boldsymbol{v}}_{dq}(k) - R_s \boldsymbol{i}_{dq}(k) - \hat{\omega}_e \mathbf{J}\, \hat{\boldsymbol{\lambda}}_{dq}(k)] \tag{5}$$

where T_s is the sampling interval. The voltage $\hat{\boldsymbol{v}}_{dq}(k)$ is estimated from the measured V_{dc} incorporating dead-time compensation. The deadbeat voltage $\boldsymbol{v}_{dq}^*(k+1)$ that drives the error in controlled variables to zero within one control cycle is given by

$$\boldsymbol{v}_{dq}^*(k+1) = R_s \boldsymbol{i}_{dq}(k) + \frac{\boldsymbol{\lambda}_{dq}^* - \boldsymbol{\lambda}_{dq}^{est}(k+1)}{T_s} + \hat{\omega}_e \mathbf{J}\, \hat{\boldsymbol{\lambda}}_{dq}^{est}(k) \tag{6}$$

where $\boldsymbol{\lambda}_{dq}^*$ is the reference flux that corresponds to the commanded reference torque T_e^* from the speed control loop. The $T_e^* \rightarrow \boldsymbol{\lambda}_{dq}^*$ relationship is obtained by superimposing a minimum λ_q over the MTPA trajectory; the need for a minimum λ_q is to aid the sensorless control as discussed in the succeeding section. The resistive term in (6) is relatively insignificant and hence the current quantities are not estimated for $k+1$ in the interest of computational efficiency.

The cost function (7) & (8) determines the voltage vector that is at the shortest Euclidean distance from the reference voltage among the six active vectors of the inverter (n = 1 .. 6) and the zero vectors (n = 0,7).

$$g(\boldsymbol{v}_j) = |\boldsymbol{v}_{dq}^*(k+1) - \boldsymbol{v}_{dq,j}| \tag{7}$$

$$\hat{\boldsymbol{v}}_{dq}(k+1) = \underset{j=0,1..7}{\operatorname{argmin}}\, g(\boldsymbol{v}_{dq,j}) \tag{8}$$

III. Sensorless Position Observer

Note that all variables represented in dq reference frame henceforth refers to the coordinates of estimated rotor position $\hat{\theta}_e = \theta_e - \tilde{\theta}_e$ where $\tilde{\theta}_e$ is the position error. Unless explicitly mentioned otherwise, the quantities correspond to the instant k. A notation of importance is $\Delta x(k) = x(k) - x(k-1)$.

A. Working principle

The proposed sensorless control is based on the instantaneous machine response upon excitation with an active voltage

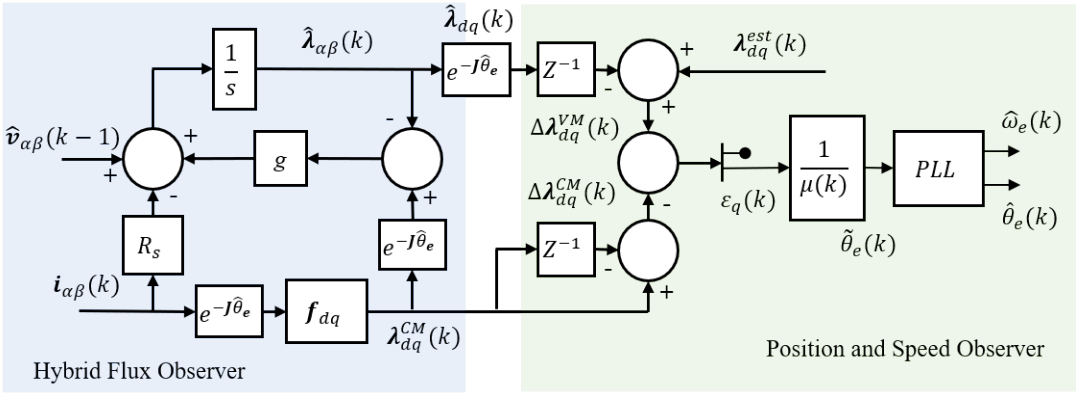


Fig. 3. Hybrid flux observer augmented with position and speed observer

vector and the precise knowledge of flux maps. The block diagram providing an overview of the observers is illustrated in Fig. 3

The principle of this approach lies in computing the rotor position from the discrepancy in estimation of stator flux ripple from voltage and current models. The error function $\boldsymbol{\epsilon}_{dq}$ is defined as

$$\boldsymbol{\epsilon}_{dq} = \Delta\boldsymbol{\lambda}_{dq}^{VM} - \Delta\boldsymbol{\lambda}_{dq}^{CM} \tag{9}$$

where $\Delta\boldsymbol{\lambda}_{dq}^{VM}$ and $\Delta\boldsymbol{\lambda}_{dq}^{CM}$ are the stator flux ripple estimate of the two models which are computed from (10) and (11) respectively.

$$\begin{aligned}\Delta\boldsymbol{\lambda}_{dq}^{VM}(k) &= T_s[\hat{\mathbf{v}}_{dq}(k-1) - R_s\mathbf{i}_{dq}(k) - \hat{\omega}_e\mathbf{J}\,\hat{\boldsymbol{\lambda}}_{dq}(k)] \\ &= \boldsymbol{\lambda}_{dq}^{est}(k) - \hat{\boldsymbol{\lambda}}_{dq}(k-1)\end{aligned} \tag{10}$$

$$\Delta\boldsymbol{\lambda}_{dq}^{CM}(k) = \boldsymbol{f}_{dq}(\boldsymbol{i}_{dq}(k)) - \boldsymbol{f}_{dq}(\boldsymbol{i}_{dq}(k-1)) \tag{11}$$

In (10), the flux estimate $\boldsymbol{\lambda}_{dq}^{est}(k) - \hat{\boldsymbol{\lambda}}_{dq}(k-1)$ is preferred respect over $\hat{\boldsymbol{\lambda}}_{dq}(k) - \hat{\boldsymbol{\lambda}}_{dq}(k-1)$ since the former is purely based on voltage model accounting for the digital delay compensation while the latter, being the output of HFO, is also influenced by the current model.

In the interest of establishing a relationship between the error function and the position error, the terms in (9) can be expressed as

$$\boldsymbol{\epsilon}_{dq} = (\mathrm{e}^{j\tilde{\theta}_e}\boldsymbol{L}^{inc}\,\mathrm{e}^{-j\tilde{\theta}_e}\Delta\boldsymbol{i}_{dq}) - (\boldsymbol{L}^{inc}\,\Delta\boldsymbol{i}_{dq}) \tag{12}$$

The matrix $\boldsymbol{L}^{inc}$ is a function of $\boldsymbol{i}_{dq}$ and is updated every control cycle. For small $\tilde{\theta}$, the expression in (12) simplifies to

$$\boldsymbol{\epsilon}_{dq} = \begin{bmatrix} -2\,l_{dq} & l_d - l_q \\ l_d - l_q & 2\,l_{dq} \end{bmatrix} \Delta\boldsymbol{i}_{dq} \cdot \tilde{\theta}_e \tag{13}$$

It is observed from (13) that the position error information is available with both the d and q axis equations; however, since $l_q < l_d$, the current ripple in i_q is higher than in i_d for equal applied voltage and consequently, less susceptible to the measurement noise and disturbances. Hence, the q axis position error estimate is found to be more reliable and is given by

$$\tilde{\theta_e} = \frac{\epsilon_q}{\mu} \tag{14}$$

where μ is a gain containing the differential inductances, and so it depends on the working point. Attention must be paid to the vicinity of the origin in dq current plane where the ribs in q axis is likely to be unsaturated. Besides the decrement in saliency, which is undesirable for sensorless control, a steep rise in l_q occurs, as can be seen Fig. 2, that is difficult to be precisely mapped. Hence, a minimum flux $\lambda_q^{min} = 0.15\,\mathrm{Vs}$ which corresponds to the knee of $\lambda_q(\boldsymbol{i}_{dq})$ saturation curve is enforced to ensure that the ribs remains saturated and that all operating points are confined to the regions of confidence of l_q.

Neglecting cross-saturation and following (13), the gain μ is expressed as

$$\mu(k) \backsimeq (l_d - l_q)\Delta i_d(k) \tag{15}$$

For machines with high l_d, the accuracy of the term $\Delta i_d(k)$ could be challenged by the resolution of current sensors and EMI disturbances. To provide a generic solution, considering approximations for low speeds, the gain is represented in terms of a known variable, $\hat{v}_d(k-1)$, as

$$\mu(k) \backsimeq (l_d - l_q)\frac{T_s}{l_d}\hat{v}_d(k-1) \tag{16}$$

Due to the fact that $\mu(k)$ appears in the denominator of (14), care must be taken for small values of $\hat{v}_d(k-1)$. If $|\hat{v}_d(k-1)| < V_{thres}$, for reasons of reliability, the position error expression (14) is not evaluated for those control cycles. A suggested value for V_{thres} is twice the dead-time phase voltage [12] to accommodate a margin of error arising from the inverter; it is expressed as

$$V_{thres} = 2 * \frac{4}{3} t_d f_s V_{dc} \tag{17}$$

where t_d is the dead-time and f_s is the sampling frequency.

If a chain of consecutive voltage vectors applied fail to meet the criteria $|\hat{v}_d(k-1)| < V_{thres}$, the position estimation is unevaluated for a continuous stretch of time leading to an eventual loss of control. To abstain from this, the cost function (7) is appended with a hard constraint as

$$g(\boldsymbol{v}_j) = |\boldsymbol{v}_{dq}^*(k+1) - \boldsymbol{v}_{dq,j}| + (n > N_{thres})\,\boldsymbol{C}_j \tag{18}$$

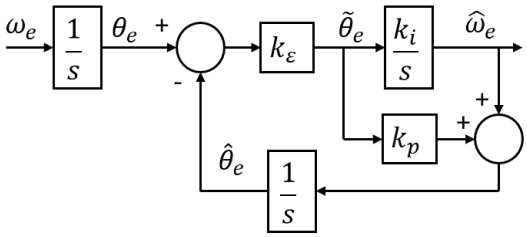


Fig. 4. Transfer function of speed and position observer

where n is the number of consecutive voltage vectors to have failed to meet the threshold. The hard constraint $\boldsymbol{C}_j$ is given by

$$\boldsymbol{C}_j = (|v_{d,j}| \leq V_{thres})\,\infty + (|v_{d,j}| > V_{thres})\,0 \tag{19}$$

Thus, when n exceeds N_{thres}, the hard constraint $\boldsymbol{C}_j$ is activated which enables only those voltage vectors that meet the threshold, hence, enforcing the position estimation. An intuitive approach to determine N_{thres} is by defining the maximum permissible step in electrical degrees between the consecutive position estimation. It is envisaged that beyond the cross-over frequency of HBO g rad/s, the well-known sensorless models based on back-emf would be dominant. Hence, considering a step of 2° electrical at g rad/s, $N_{thres} = 5$ is obtained.

B. PLL and calibration of tracking loop

The position observer comprises of a standard PLL with a PI controller in cascade with a integrator. The speed is observed at the output of PI integrator. No additional filters are required. The transfer function of the observers are shown in the Fig. 4 where k_ϵ is the term relating the real position error to the estimate error. Under ideal conditions and precise modeling, $k_\epsilon = 1$.

The closed loop transfer function of the position observer is given by

$$\frac{\hat{\theta}_e(s)}{\theta_e(s)} = \frac{sk_p + k_i}{s^2 + sk_p + k_i} \tag{20}$$

It can be deduced that the bandwidth of position observer $\Omega_{\theta_e} \backsimeq k_p$. In order to have a phase margin $> 45^\circ$, the inequality $k_i/k_p < k_\epsilon k_p$ must be satisfied. Further, examining the poles of the characteristic equation, the condition for the existence of non-imaginary poles is

$$k_i/k_p \leq k_p/4 \tag{21}$$

This imposes a much stringent inequality, respecting which ensures a higher phase margin.

The transfer function for the speed observer in (22) is seen to possess the same poles as the position observer and hence the former discussion for non-imaginary poles applies.

$$\frac{\hat{\omega}_e(s)}{\omega_e(s)} = \frac{k_i}{s^2 + sk_p + k_i} \tag{22}$$

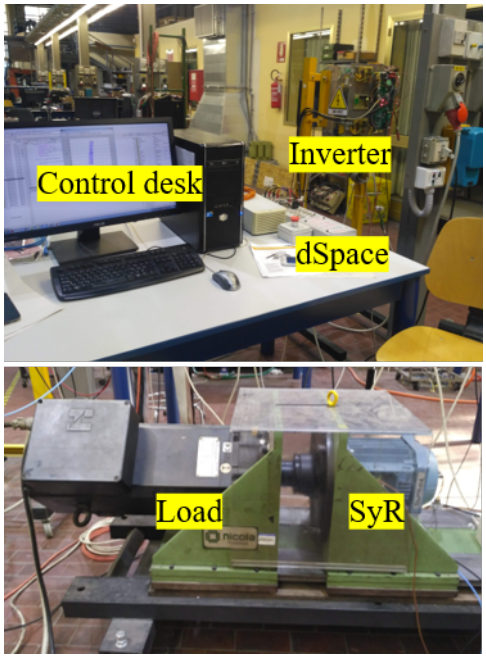


Fig. 5. Experimental testbench

Incorporating (21) in (22), the maximum permissible bandwidth of the speed observer is $\Omega_{\omega_e} \leq 0.5\,\Omega_{\theta_e}$; it must be less than half of the position observer.

Unlike the high frequency injection scheme where the bandwidth of the position observer is limited by the LPF of the demodulation stage, this injectionless structure has no such restriction. $\Omega_{\theta_e} = 100\,\text{Hz}$ is chosen; higher values, though stable, do not have any discernible impact. To permit sufficient margin of error and robustness, $\Omega_{\omega_e} = 20\,\text{Hz}$ is chosen. For the purpose of calibration, $k_\epsilon = 1$ is considered; the corresponding k_p and k_i are calculated from the former expressions. The speed control loop is recommended to have less than one fourth the bandwidth of speed observer.

IV. Experimental Results

A. Testbench setup

The proposed sensorless scheme has been validated experimentally on a 1 kW SyR motor. The control was implemented on a dSpace DS1103 running at a sampling frequency of 10 kHz. The load is an auxiliary drive connected to the shaft. A picture of the setup is shown in Fig. 5. The parameters of the SyR under test are tabulated in Table I.

B. Results and discussion

In the following experimental results, the SyR motor was closed loop speed controlled while the auxiliary drive was applying an arbitrary load torque. The robustness of the proposed algorithm is tested under torque and speed transients as well as steady-states.

TABLE I
MOTOR PARAMETERS

Parameters	Symbol	Values	Units
Rated Power	P_n	1	kW
Rated Voltage	V_n	340	V
Rated Speed	ω_n	1500	rpm
Rated Current	I_n	3.6	A
Rated Torque	T_n	7.1	Nm
Pole pairs	p	2	-
Stator Resistance	R_s	4.5	Ω
Shaft Inertia	J	0.04	kgm^2

1) Response to speed reversal: The performance of the drive for a sharp speed reversal is shown in Fig. 6. At $t = 0s$, the speed is reversed from -100 rpm to $+100$ rpm under no load. The position estimation is stable during the transient and the error is observed to be less than $4°$. The speed is seen to marginally overshoot the reference which can be improved by reducing k_i of the speed regulator at the cost of compromising stiffness to load disturbances.

2) Response to torque step: The torque transient test is performed at zero speed which is often the most challenging region of operation. A torque step of $0 \rightarrow T_n$ Nm and $T_n \rightarrow 0$ Nm is imposed on the auxiliary drive at $t = 0.9s$ and $t = 3.3s$ respectively as shown in Fig. 7. A sag in the speed of around 120 rpm is observed which is in accordance with the design parameters ($\backsimeq T_n/k_p$). The high bandwidth is evident from the fast convergence of the position observer to step change in torque. A small steady-state error in the position estimate is observed which is attributed to the dead-time and non-linear effects of the inverter that gains influence at zero/low speeds. Such position error is around $4°$.

3) Steady-state response at low speeds: To ascertain the stability of control at low speeds, a slow ramping speed reference is considered under no load to study the steady-state response. The speed is ramped from -50 rpm to +50 rpm over a span of 2s, as shown in Fig. 8. The position error is discerned to be almost zero throughout region of investigation.

V. CONCLUSION

This work has presented a sensorless control technique at zero and low speeds region without adopting high frequency signal injection. Exploiting saliency, the position estimate is extracted from the switching actuation of model predictive control. Since it relies only on the q axis excitations, it is not merely limited to low inductance machines but has the potential to be a generic solution. It benefits from a high bandwidth position observer due to the absence of filters and it requires minimal calibration effort. Guidelines for the tuning of regulators have been addressed. The proposed technique was validated on a 1 kw SyR experimental test-bench. Owing to the large bandwidth, the position error is confined within $\pm 5°$ electrical during sharp transients of speed and torque variations. It was found to be stable in the desired operation region.

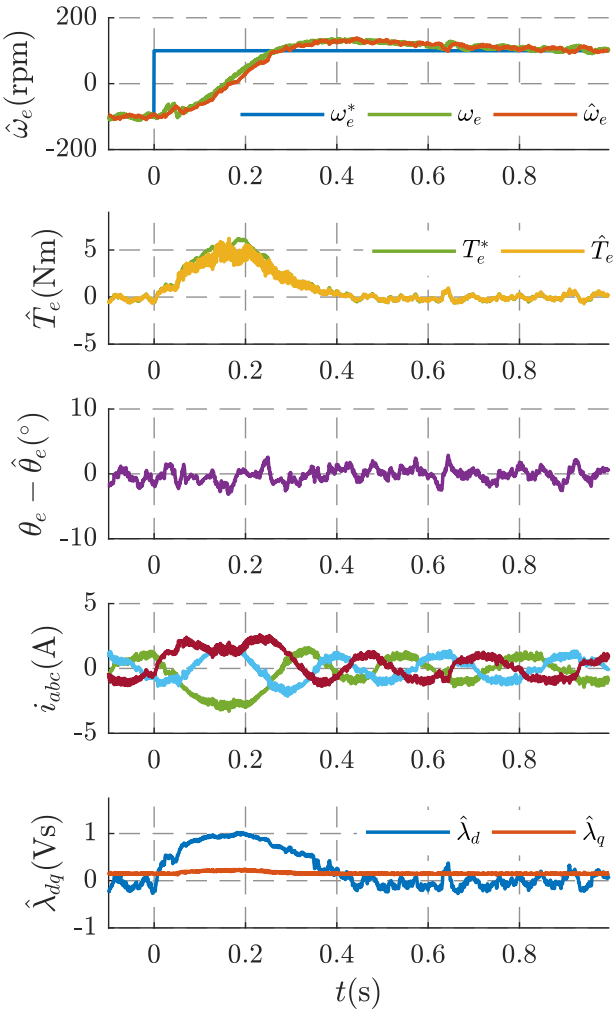


Fig. 6. Transient response to speed reversal: ± 100 rpm

REFERENCES

[1] S. C. Agarlita, I. Boldea, and F. Blaabjerg, "High-frequency-injection-assisted 'active-flux'-based sensorless vector control of reluctance synchronous motors, with experiments from zero speed," *IEEE Transactions on Industry Applications*, vol. 48, no. 6, pp. 1931–1939, 2012.

[2] A. Yousefi-Talouki, P. Pescetto, G. Pellegrino, and I. Boldea, "Combined Active Flux and High Frequency Injection Methods for Sensorless Direct Flux Vector Control of Synchronous Reluctance Machines," *IEEE Transactions on Power Electronics*, vol. 33, no. 3, pp. 1–1, 2017.

[3] F. Briz, M. W. Degner, J. Chen, R. Qu, J. Li, M. W. Degner, F. Briz, F. Betin, G. A. Capolino, D. Casadei, B. Kawkabani, R. I. Bojoi, L. Harnefors, E. Levi, L. Parsa, and B. Fahimi, "Rotor Position Estimation," *IEEE Industrial Electronics Magazine*, vol. 5, no. 2, pp. 24–36, 2011.

[4] M. Hofer, M. Nikowitz, and M. Schroedl, "Sensorless control of a reluctance synchronous machine in the whole speed range without voltage pulse injections," *2017 IEEE 3rd International Future Energy Electronics Conference and ECCE Asia, IFEEC - ECCE Asia 2017*, pp. 1194–1198, 2017.

[5] R. Morales-Caporal and M. Pacas, "Suppression of saturation effects in a sensorless predictive controlled synchronous reluctance machine based

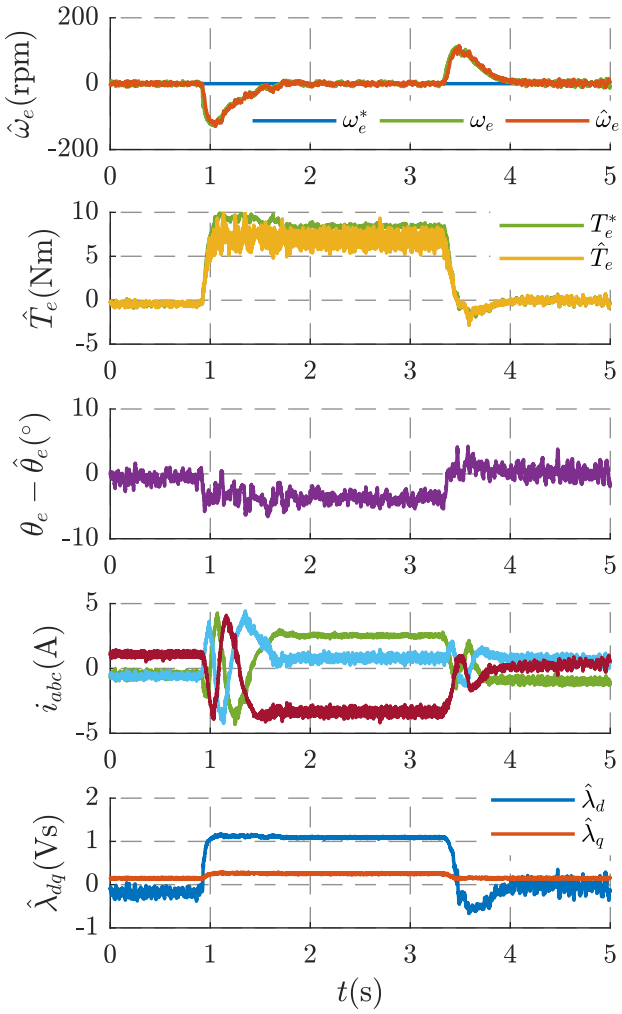


Fig. 7. Transient response for step change in torque: $\pm T_n$ Nm

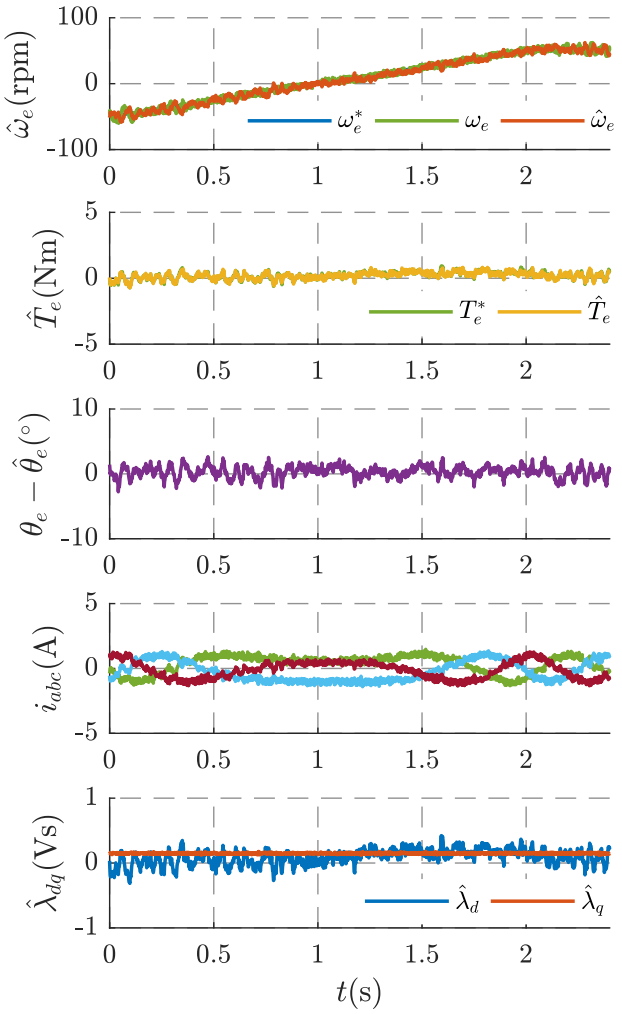


Fig. 8. Steady-state response in low speeds region: ± 50 rpm

on voltage space phasor injections," *IEEE Transactions on Industrial Electronics*, vol. 58, no. 7, pp. 2809–2817, jul 2011.

[6] F. J. Barnard, W. T. Villet, and M. J. Kamper, "Hybrid Active-Flux and Arbitrary Injection Position Sensorless Control of Reluctance Synchronous Machines," *IEEE Transactions on Industry Applications*, vol. 51, no. 5, pp. 3899–3906, 2015.

[7] Y. D. Yoon, S. K. Sul, S. Morimoto, and K. Ide, "High-bandwidth sensorless algorithm for AC machines based on square-wave-type voltage injection," *IEEE Transactions on Industry Applications*, vol. 47, no. 3, pp. 1361–1370, 2011.

[8] M. Preindl and E. Schaltz, "Sensorless Model Predictive Direct Current Control Using Novel Second-Order PLL Observer for PMSM Drive Systems," *IEEE Transactions on Industrial Electronics*, vol. 58, no. 9, pp. 4087–4095, 2011.

[9] P. Landsmann, D. Paulus, P. Stolze, and R. Kennel, "Saliency based encoderless Predictive Torque Control without signal injection for a reluctance synchronous machine," pp. S1–10–S1–17, 2010.

[10] L. Rovere, A. Formentini, A. Gaeta, P. Zanchetta, and M. Marchesoni, "Sensorless Finite-Control Set Model Predictive Control for IPMSM Drives," pp. 5921–5931, 2016.

[11] S. Nalakath, Y. Sun, M. Preindl, and A. Emadi, "Optimization-Based Position Sensorless Finite Control Set Model Predictive Control for IPMSMs," *IEEE Transactions on Power Electronics*, vol. 33, no. 10, pp. 8672–8682, 2018.

[12] G. Pellegrino, P. Guglielmi, E. Armando, and R. I. Bojoi, "Self-commissioning algorithm for inverter nonlinearity compensation in sensorless induction motor drives," *IEEE Transactions on Industry Applications*, vol. 46, no. 4, pp. 1416–1424, 2010.